Available online at www.sciencedirect.com
SCIENCE DIRECT®
Applied Acoustics 66 (2005) 1278–1308
applied acoustics
www.elsevier.com/locate/apacoust

Computation of internal aerodynamic noise from a quick-opening throttle valve using frequency-domain acoustic analogy

Jewook Ryu [a,1], Cheolung Cheong [b,*], Sungtae Kim [a,1], Soogab Lee [c,2]

[a] *School of Mechanical and Aerospace Engineering, Seoul National University, Building 301-1214, Seoul National University, Seoul 151-742, Korea*
[b] *Acoustics and Vibration Group, Division of Physical Metrology, Korea Research Institute of Standards and Science, Daejeon 305-340, Korea*
[c] *School of Mechanical and Aerospace Engineering, Seoul National University, Building 301-1303, Shilim-Dong, Kwanak-Gu, Seoul 151-742, Korea*

Received 30 April 2003; received in revised form 15 November 2004; accepted 4 April 2005
Available online 23 May 2005

Abstract

Recently, plastic products in air-intake parts of automotive engines have become very popular due to advantages that include reduced weight, constricted cost, and lower intake air temperature. However, flow-induced noise in air-intake parts becomes a more serious problem for plastic intake-manifolds than for conventional aluminum-made manifolds. This is due to the fact that plastic manifolds transmit more noise owing to their lower material density. Internal aerodynamic noise from a quick-opening throttle valve is computed by using a frequency-domain acoustic analogy, which is based on the integral formula derived by using the General Green Function, Lighthill's acoustic analogy and Curle's extension of Lighthill's. The integral formula is arranged in such a manner that allows a frequency-domain acoustic signal to be predicted at any location in a duct through the use of unsteady flow data in space and time,

* Corresponding author. Tel.: +82 42 868 5793; fax: +82 42 868 5643.
E-mail address: ccheong@kriss.re.kr (C. Cheong).
[1] Tel.: +82 (0)2 880 1902.
[2] Tel.: +82 (0)2 880 7384; fax: 82 (0)2 875 4360.

0003-682X/$ - see front matter
doi:10.1016/j.apacoust.2005.04.002

which can be obtained by applying Computational Fluid Dynamics techniques. The prediction of the acoustic pressure level from the quick-opening throttle valve shows good agreement with actual measurement. Through the detailed analysis of the flow-noise generation mechanism it was found that the anti-vortex lines, formed behind the throttle valve during the quick-opening behavior, feed the large-scale coherent turbulence and, as a result, play a crucial role in generating the dipolar sound from unsteady loading of the quick-opening throttle valve. From this, it can be inferred that the low-noise design of the throttle-duct system can be made by using this concept to break the large-scale vortex structure.

Keywords: Valve noise; Engine intake noise; Aeroacoustics; Acoustic analogy

1. Introduction

Recently, plastic products in air-intake parts have become popular with the advancement of the modularization techniques of engine parts. However, plastic intake manifolds have lower sound transmission loss than customary aluminum-made intake manifolds because of their lower material density. This low transmission loss property of plastic intake manifolds focuses attention on flow-induced noise from a throttle valve in a quick-opening status. Nakase et al. [1] performed experiments on the noise from a quick-opening throttle valve and numerical analysis on the flow field around the throttle valve, and tried to relate the turbulence characteristics to generated noise. However, their research is not based on robust aeroacoustic theory, but an almost ad hoc method. Furthermore, the origin of the noise generation mechanism had not been clarified. The physical processes, which normally cause for this type of flow noise to be produced, include turbulent fluid motion and relative motion of the throttle valve to the airflow. The strong turbulent flow is generated by high-speed airflow in the gap between the throttle valve and the inner-surface of the conduit containing the throttle valve. This turbulent velocity can be modelled as quadrupole sources. The relative motion of the throttle valve to the airflow and the vorticity of the turbulence induce the unsteady force on the flow. This unsteady force can be classified into dipole sources.

Generation and propagation of flow-induced noise in internal flows have quite different aspects than those in external flows. From a physical standpoint of sound generation and propagation, acoustic waves radiated from noise sources in the external flow are affected only by the interference of noise sources themselves, while those in the internal flow are influenced by the interference between the wall and noise sources as well as that of noise sources themselves. The interference of the wall and noise sources leads to modal solutions to internal acoustic fields.

Previous works on internal aeroacoustics can be categorized into two types: purely theoretical and hybrid approaches. Theoretical approaches for the analysis of internal flow noise can be categorized into two types. The first is theoretical approaches of which the main purpose is to find the principal features of acoustic fields caused by source distributions in ducts by using well-established mathematical theories. This group includes the works of Doak [2] and Davies and Ffowcs Williams

[3]. The second theoretical approach for internal flow noise is the family of theoretical attempts made to establish scaling laws that relate the sound power radiated to the geometry and flow parameters involved. This group includes the works of Gordon [4,5], Nelson and Morfey [6], and Oldham and Ukpoho [7]. However, it is evident that the analytic methods have some difficulties in serving as general design tools due to their limitations in the application arena. Hybrid approaches for the internal aerodynamic noise mean that the noise predictions are carried out by combining the acoustic analogy and the previously calculated flow data as input to the acoustic analogy. While there have been several works [8,9] done in this category, scarcely any work has been done on the internal aerodynamic noise from quickly moving throttle valves.

The main objective of the present work is to investigate the main features of noise from a quick-opening throttle valve and then to find the hidden noise generation mechanism, which provides the basic philosophy to low-noise design. The hybrid model is utilized in predicting internal aerodynamic noise. This model is based on the integral formula derived from the inhomogeneous wave equation of Lighthill's acoustic analogy [10] and Curle's extension [11] of Lighthill's by using the General Green Function. The integral formula is arranged in such a manner that the frequency-domain acoustic signal can be predicted at any location in a duct by using the unsteady flow data in space and time, which can be obtained by using the Computational Fluid Dynamic (CFD) techniques. Fig. 1 shows the schematic diagram of the computational procedure for predicting the internal aerodynamic noise from a quick-opening throttle valve.

It is noted that preliminary aspects of this work has been reported in the paper [12] presented for the 18th International Congress on Acoustics. The current paper is an extended and finalized version of the related research work.

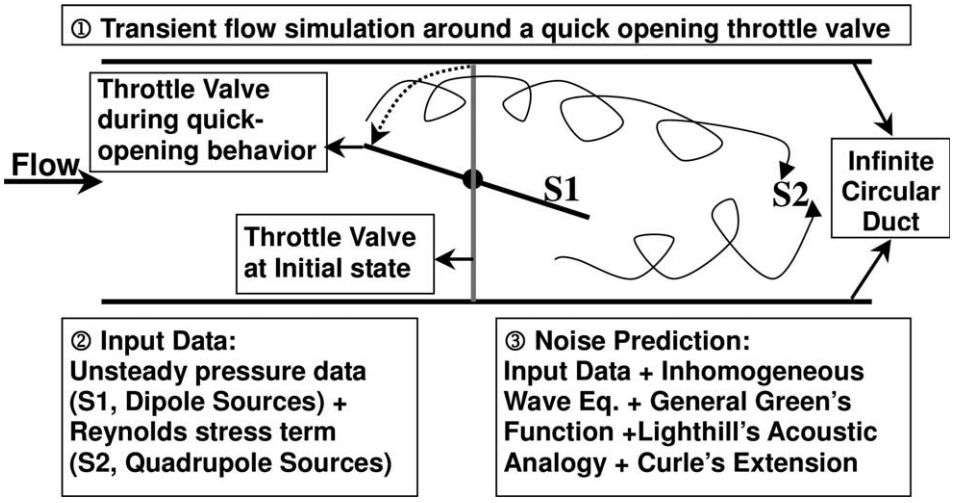

Fig. 1. Diagram of the computational procedure of the internal aerodynamic noise from a quick-opening throttle valve.

2. Fundamental formulations

2.1. Equation for sound field

Coordinates are chosen with the origin on the center of the throttle valve, y_1 being coordinates in the flow-stream direction, y_2 in the rotational axis of the throttle valve and y_3 in the direction normal to the y_1- and y_2-axis. The problem of sound generated by a flow and an obstacle in a duct can be treated by replacing the solid obstacle by a distribution of dipole sources and the turbulence by a distribution of quadrupole sources, respectively. Then, the equation governing the sound field in the duct is Lighthill's form and Curle's extension from Lighthill's as follows.

$$\left\{\nabla^2 - \frac{1}{c^2}\frac{\partial^2}{\partial\tau^2}\right\}p(y_k,t) = \left(\frac{\partial}{\partial y_i}\right)[f_i(y_k,t)] - \left(\frac{\partial}{\partial y_i}\right)\left[\frac{\partial T_{ij}}{\partial y_j}\right], \tag{1}$$

where p is the pressure, τ is time, c is the speed of sound, f_i is force per unit volume and T_{ij} is Lighthill's stress tensor. T_{ij} denotes the expression $\rho u_i u_j + [(p-p_0) - c^2(\rho-\rho_0)]\delta_{ij} - e_{ij}$, where δ_{ij} is the Kronecker delta, u_i is the velocity in the y_i-direction and e_{ij} is the viscous stress tensor. Assuming that the viscous stress and the entropy fluctuation are negligible within the moving fluid, Lighthill's stress tensor is approximately equal to $\rho u_i u_j$. It is also assumed that the modeled source terms on the right-hand side of Eq. (1) act over a limited area of the duct.

In addition to satisfying Eq. (1), the solution must satisfy appropriate boundary conditions as follows: All waves are outgoing at infinity, and the normal velocity vanishes at the walls. At the hard walls, the normal component of the particle velocity must vanish and the boundary condition on the pressure at the duct walls is

$$\frac{\partial p}{\partial n} = 0, \tag{2}$$

where n is the normal to the wall. Eq. (1) can be solved by means of utilizing a Green's function $G(\mathbf{x}, t|\mathbf{y}, \tau)$ defined as the solution of

$$\nabla^2 G - \frac{1}{c^2}\frac{\partial^2 G}{\partial\tau^2} = \delta(\mathbf{x}-\mathbf{y})\delta(t-\tau) \tag{3}$$

with $\partial G/\partial n = 0$ on the boundaries where $\mathbf{x}$ is a coordinate associated with the observation point and $\mathbf{y}$ is a coordinate associated with the source point. By using Eq. (3), the time-domain acoustic pressure from internal flow can be expressed as

$$p(\mathbf{x},t) = c^2\rho(\mathbf{x},t) = \int_v\int_t G(\mathbf{x},t|\mathbf{y},\tau)\left\{\frac{\partial f_i(\mathbf{y},\tau)}{\partial y_i} - \frac{\partial^2 T_{ij}(\mathbf{y},\tau)}{\partial y_i \partial y_j}\right\}\mathrm{d}\mathbf{y}\,\mathrm{d}\tau, \tag{4}$$

where the volume integral is spread out throughout the entire space and the time integral ranges from $-\infty$ to ∞. The Green function chosen is an exact form, and with the boundary conditions specified, ensures that the solution does not involve any surface integrals. The detailed derivation of the Green function of Eq. (3) is given in Appendix A. Eq. (4) can be written by inserting Eq. (A.9) into Eq. (4) as

$$p(\mathbf{x},t) = c^2\rho(\mathbf{x},t)$$
$$= \frac{\mathrm{i}}{4\pi}\sum_{m,n=0}^{\infty}\frac{\Psi^*_{m,n}(x_2,x_3)}{\Gamma_{m,n}}\int_v \mathrm{d}\mathbf{y}\int_{-\infty}^{\infty}\mathrm{d}\tau\int_{-\infty}^{\infty}\mathrm{d}\omega\Psi_{m,n}(y_2,y_3)$$
$$\times\frac{\exp\{\mathrm{i}k_{mn}|x_1-y_1|-\mathrm{i}\omega(t-\tau)\}}{k_{m,n}}\left\{\frac{\partial f_i(\mathbf{y},\tau)}{\partial y_i}-\frac{\partial^2 T_{ij}(\mathbf{y},\tau)}{\partial y_i\partial y_j}\right\}. \tag{5}$$

The term k_{mn}, defined by Eq. (A.9), denotes the (m, n) mode of the wave number in the streamwise direction. For propagating wave motion, the wave number must be real, which should be above the cut-off frequency, denoted by $\omega_{mn} = ck_{mn}$. For a frequency of less than the cut-off frequency, k^2_{mn} is negative and the pressure in that mode decays exponentially away from the source. A similar form of the integral equation has been used in previous theoretical studies [2,3,6].

2.2. Rearrangement for semi-analytic algorithm

In this section, Eq. (5) is rearranged such that frequency-domain acoustic pressure at an arbitrary position in a duct can be computed by using unsteady flow data in time and space, which are provided by applying the CFD techniques.

First, consider the Fourier transform of Eq. (5) on the time t at position $\mathbf{x}$, then the Fourier transform of pressure p at frequency ω can be described as follows:

$$p(\mathbf{x},\omega) = \frac{\mathrm{i}}{2}\sum_{m,n=0}^{\infty}\frac{\Psi^*_{m,n}(x_2,x_3)}{\Gamma_{m,n}}\int_v \mathrm{d}\mathbf{y}\int_{-\infty}^{\infty}\mathrm{d}\tau\Psi_{m,n}(y_2,y_3)$$
$$\times\frac{\exp\{\mathrm{i}k_{mn}|x_1-y_1|+\mathrm{i}\omega\tau)\}}{k_{m,n}}\left\{\frac{\partial f_i(\mathbf{y},\tau)}{\partial y_i}-\frac{\partial^2 T_{ij}(\mathbf{y},\tau)}{\partial y_i\partial y_j}\right\}. \tag{6}$$

In order to combine the above equation with given flow data in space and time, Eq. (6) is rewritten as follows:

$$p(\mathbf{x},\omega) = \frac{\mathrm{i}}{2}\sum_{m,n=0}^{\infty}\frac{\Psi^*_{m,n}(x_2,x_3)\exp\{\mathrm{i}k_{mn}x_1\}}{\Gamma_{m,n}}\{\mathbf{D}_{mn}(\omega)+\mathbf{Q}_{mn}(\omega)\}, \tag{7}$$

where

$$\mathbf{D}_{mn}(\omega) = \int_{-\infty}^{\infty}\int_V \Psi_{m,n}(y_2,y_3)\frac{\exp\{-\mathrm{i}k_{mn}y_1+\mathrm{i}\omega\tau)\}}{k_{m,n}}\left\{\frac{\partial f_i(\mathbf{y},\tau)}{\partial y_i}\right\}\mathrm{d}v\,\mathrm{d}\tau \tag{8}$$

and

$$\mathbf{Q}_{mn}(\omega) = -\int_{-\infty}^{\infty}\int_V \Psi_{m,n}(y_2,y_3)\frac{\exp\{-\mathrm{i}k_{mn}y_1+\mathrm{i}\omega\tau)\}}{k_{m,n}}\left\{\frac{\partial^2 T_{ij}(\mathbf{y},\tau)}{\partial y_i\partial y_j}\right\}\mathrm{d}v\,\mathrm{d}\tau. \tag{9}$$

Here, $\mathbf{D}_{mn}$ denotes the (m, n) mode components related to dipole sources and $\mathbf{Q}_{mn}$ to quadrupole sources. By applying the divergence theorem to Eqs. (8) and (9) with integral space enough to cover the entire field at the boundary on which the sources disappear, Eqs. (8) and (9) can be rewritten as follows, respectively.

$$\mathbf{D}_{mn}(\omega) = -\frac{1}{k_{m,n}} \int_{-\infty}^{\infty} \int_{V} f_i(\mathbf{y},\tau) \frac{\partial}{\partial y_i} \{ \Psi_{m,n}(y_2,y_3) \exp\{-\mathrm{i}k_{mn}y_1 + \mathrm{i}\omega\tau)\}\} \,\mathrm{d}v\,\mathrm{d}\tau \tag{10}$$

and

$$\mathbf{Q}_{mn}(\omega) = -\frac{1}{k_{m,n}} \int_{-\infty}^{\infty} \int_{V} T_{ij}(\mathbf{y},\tau) \frac{\partial}{\partial y_i \partial y_j} \{ \Psi_{m,n}(y_2,y_3) \exp\{-\mathrm{i}k_{mn}y_1 + \mathrm{i}\omega\tau)\}\} \,\mathrm{d}v\,\mathrm{d}\tau. \tag{11}$$

Unsteady data provided by flow simulations can be used to calculate the f_i term of Eq. (10) and the T_{ij} term of Eq. (11). For a cylindrical duct, the eigenfunction of Eqs. (10) and (11) can be expressed as

$$\Psi_{m,n} = J_m(\kappa_{m,n} r)\mathrm{e}^{-\mathrm{i}m\theta}, \tag{12}$$

where $r = \sqrt{y_2^2 + y_3^2}$ and $\theta = \tan^{-1}(y_2/y_3)$. Here, J_m is m-th Bessel function and κ_{mn} is the n-th root of the following equation:

$$J'_m(\kappa_{m,n} r_d) \equiv \left.\frac{\mathrm{d}J_m(x)}{\mathrm{d}x}\right|_{x=\kappa_{m,n} r_d} = 0. \tag{13}$$

From Eq. (A.4), the following equation can be obtained:

$$\Gamma_{mn} = \pi\left(r_d^2 - \frac{m^2}{\kappa_{mn}^2}\right) J_m^2(\kappa_{mn} r_d). \tag{14}$$

Insertion of Eq. (12) into Eqs. (10) and (11) leads to

$$\mathbf{D}_{mn}(\omega) = \frac{1}{k_{m,n}} \int_{-\infty}^{\infty} \int_{V} f_i(\mathbf{y},\tau) \frac{\partial}{\partial y_i} \left\{ J_m(\kappa_{m,n} r)\mathrm{e}^{-\mathrm{i}(k_{mn}y_1 + m\theta)} \right\} \exp\{\mathrm{i}\omega\tau\} \,\mathrm{d}v\,\mathrm{d}\tau \tag{15}$$

and

$$\mathbf{Q}_{mn}(\omega) = \frac{1}{k_{m,n}} \int_{-\infty}^{\infty} \int_{V} T_{ij}(\mathbf{y},\tau) \frac{\partial}{\partial y_i \partial y_j} \left\{ J_m(\kappa_{m,n} r)\mathrm{e}^{-\mathrm{i}(k_{mn}y_1 + m\theta)} \right\} \exp\{\mathrm{i}\omega\tau\} \,\mathrm{d}v\,\mathrm{d}\tau. \tag{16}$$

It is convenient to convert the rectangular coordinate system in Eqs. (15) and (16) into a cylindrical coordinate system because the eigenfunction of Eqs. (15) and (16) is expressed in the cylindrical coordinate system. Coordinate transformation is described in greater detail in Appendix B.

3. Intake noise from throttle valve in an automotive engine

The semi-analytic model, which was discussed in the previous section, is applied to the throttle valve noise problem described schematically in Fig. 1. Fig. 2 shows the behavior of throttle valve angle and its corresponding acoustic pressure, as measured when the throttle is opened quickly. For this measurement, the airflow is suctioned

through the outlet of the manifold at the volume flow rate corresponding to that of a 2000 cc engine at the operating condition of 1500 rpm, and the throttle valve angle was changed from fully closed (5°) to wide-open (90°) in 0.227 s. This measurement shows that the strong noise signal is generated when the throttle is opened within the 20–50° angle-range.

3.1. Analysis of airflow

In this section, the numerical results and discussion on the airflow produced by the quick-opening throttle valve are presented. The numerical method used for viscous flow simulation is based on the unstructured grid finite volume method. The Quadratic Upstream Interpolation for Convective Kinematics (QUICK) scheme [13] is used for spatial discretization, the fully implicit scheme [14] for time discretization, and the solution algorithm is based on the PISO method [15]. To numerically analyze a three-dimensional flow, the flow fields must be represented by a calculation mesh. The flow field configuration changes as the throttle valve continues opening. Therefore, several calculation meshes are required for the corresponding throttle valve angles in order to numerically analyze airflow during the whole range of throttle operation. To overcome this difficulty, the calculation area is divided into the duct section and the spherical section. The spherical section contains baffle cells modeling the throttle valve and allows for the rotation of the baffle cell, i.e., the motion of the throttle valve. Fig. 3 shows the calculation meshes where the entire spherical section is rotated about the axis of the throttle valve. This makes it comparatively easy to prepare a calculation mesh for each throttle valve angle, which enables numerical analysis to be performed at every airflow configuration change. The moving boundary between the duct and spherical meshes is accommodated with the arbitrary sliding interface method [16]. By using the symmetric geometry of the concerned problem, we can analyze only half the section of the throttle, and as a result, calculation time is reduced. The mesh for the simulation contains 26,355 nodes and 22,820 hexahedral elements.

It takes 0.227 s for the throttle to open from the fully a closed position to the fully open position. The opening time is determined to meet the experimental condition. The fluid is assumed to be a compressible viscous flow with the properties of air. To reproduce the experimental conditions as closely as possible, the measured values of static pressure at points upstream and downstream of the throttle valve are used as inflow and outflow boundary conditions. The static pressure at the inlet plane is observed to be kept almost constantly at atmospheric pressure, while the pressure on the exit side is observed to increase steadily from low pressure to nearly atmospheric pressure during the quick opening of the throttle valve. Fig. 4 shows the measured static pressure on the exit side. Fig. 5 shows the boundary conditions used for the simulation. Flow simulation is carried out with the time step $\Delta t = 0.0002$ [s], which means that we can obtain flow data sets at the 1135 different time steps from each time interval from 0 to 0.227 s time-interval, i.e., from the 5° to 90° angles-range. In the following, the airflow characteristics are analyzed at four throttle open angles;

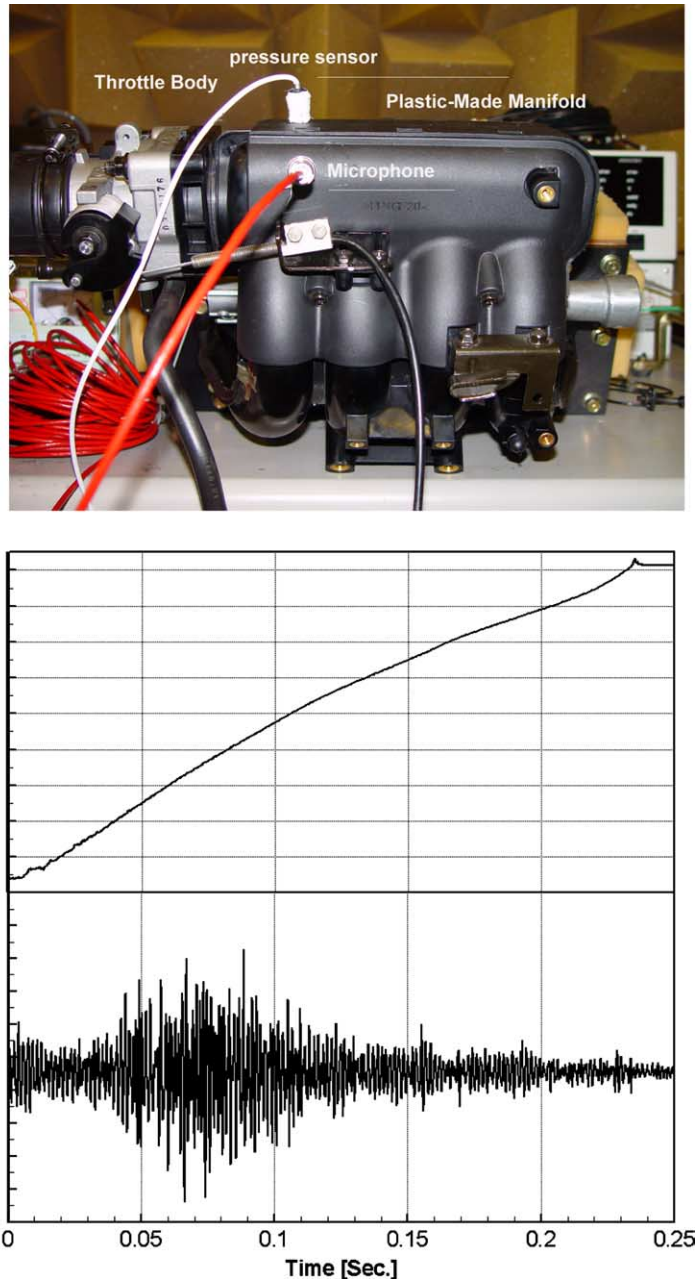

Fig. 2. Throttle body and manifold for actual measurement, behavior of throttle angle and flow-induced noise from the quick-opening throttle valve.

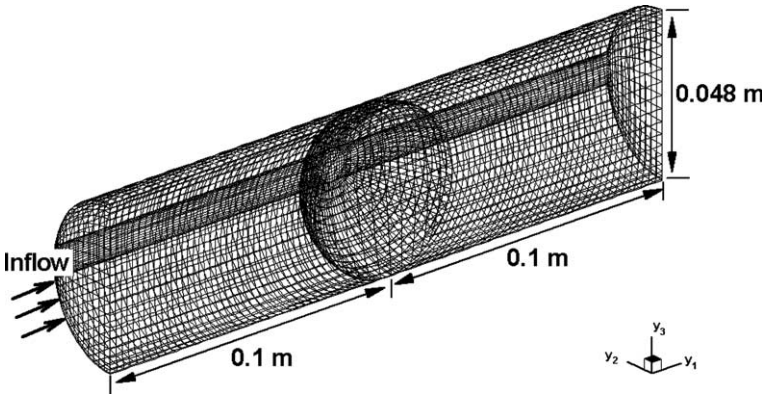

Fig. 3. Mesh for calculation and dimensions for the throttle valve and the conduit.

20°, 30°, 40° and 50°, which are chosen based on the experimental observation that the strong acoustic wave is produced between the 20° and 50° angle range.

Figs. 6(a) and (b) show the distribution of velocity vectors for the airflow at a longitudinal cross-section passing through the duct axis, with airflow from left to right, when the throttle is opened to 20°. The flow velocity vector diagrams show very fast airflow in the upper part of the throttle. This airflow consists of two streams, one of which turns back towards the throttle valve, and the other that whirls into the lower

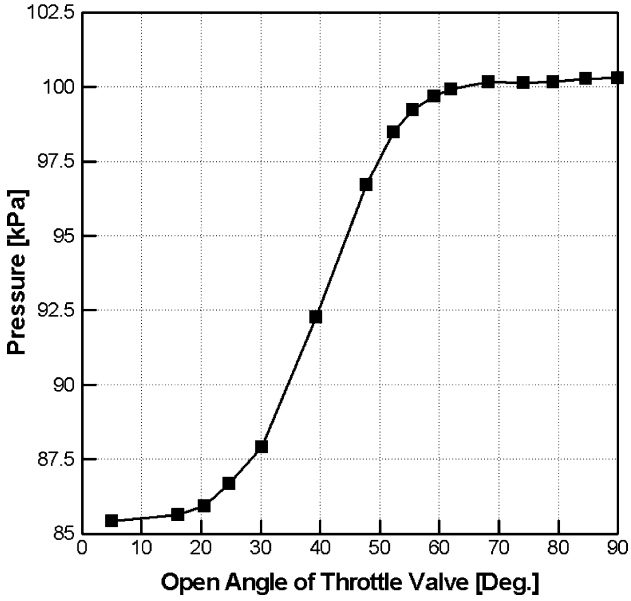

Fig. 4. Measured pressure history at the outlet of the duct for the numerical simulation.

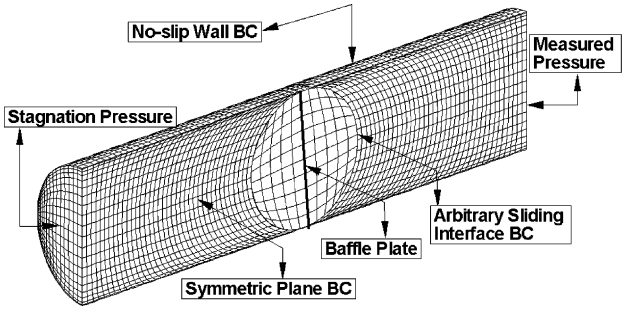

Fig. 5. Applied boundary conditions for the numerical simulation.

part of the throttle valve. Observing the airflow along a cross-section perpendicular to the duct axis as shown in Fig. 6(c), we can see a swirling flow where the airflow in the central area of the duct travels from the upper part to the lower part of the throttle, and then, goes upwards to the upper part along the inner-wall of duct. In the region further downstream, Fig. 6(d), there are three vortex flows (two are distinct and one is ambiguous). It means that, at this initial stage of throttle valve opening, the vortex line formed just behind the throttle valve along the duct is divided into several lines in the downstream region. Fig. 7 shows the contours of the static pressure and turbulence kinetic energy. The pressure contour diagram shows that, at a relatively small open angle mimicking the initial stage of throttle valve opening, the pressure in the area downstream is low, indicating that the airflow does not reach the exit of the conduit. Turbulence kinetic energy k, calculated by the k–ϵ model, has a large value

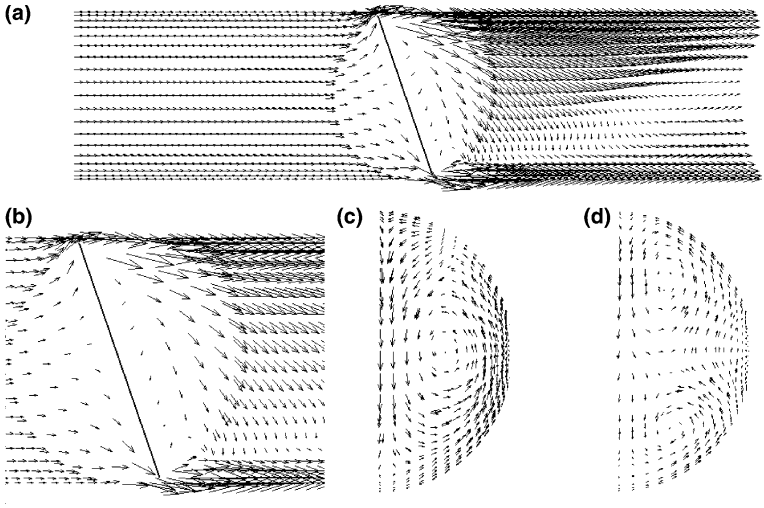

Fig. 6. Velocity distribution of airflow when the throttle valve is opened to 20° (maximum velocity = 141.3 m/s): (a) at the plane $y_2 = 0$, (b) zoomed plot, (c) at the plane $y_1 = 0.03$ m and (d) at the plane $y_1 = 0.06$ m.

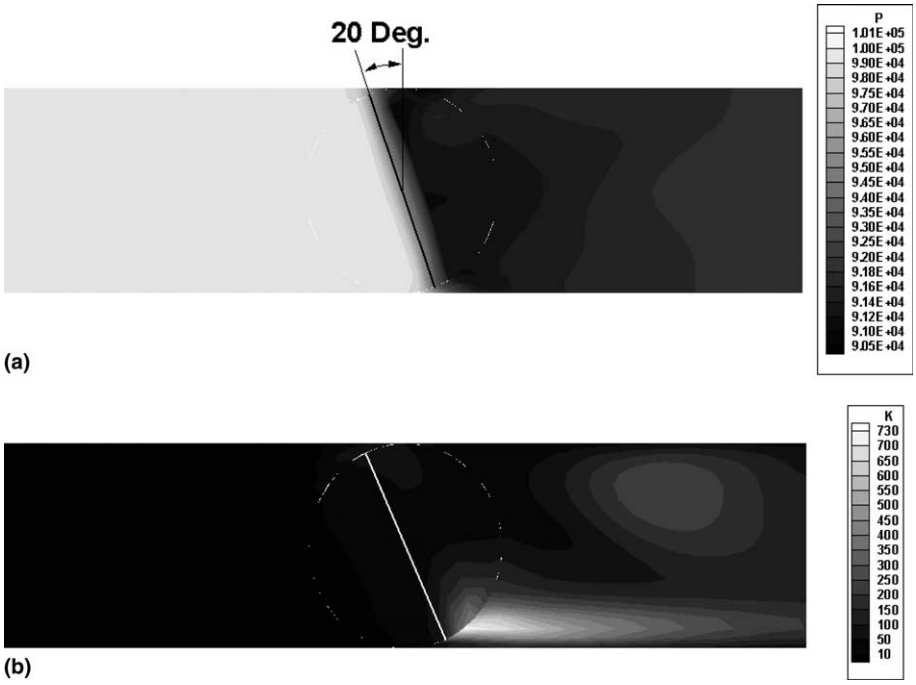

Fig. 7. Distributions of (a) pressure and (b) turbulence kinetic energy at the symmetric plane $y_2 = 0$ at the open angle of 20°.

over a wide area downstream from the throttle valve and the maximum region is located on the lower part of the duct in the symmetric plane. It is noted that the unsteady pressure on the surface of the throttle valve and turbulent velocities in the flow are used to calculate the f_i and T_{ij} terms of Eqs. (15) and (16), which are used with Eq. (7) to predict frequency-domain acoustic pressures.

Figs. 8(a) and (b) show the distribution of velocity vectors for airflow at a longitudinal cross-section passing through the duct axis when the throttle is opened to an angle of 30°. The flow velocity vector diagrams show that a very fast airflow passes through the upper and lower parts of the throttle. In the area 30–60 mm downstream from the throttle valve, the streams from both the upper and lower parts of the throttle mix and merge in the lower part of the duct. The vector diagram of a cross-section perpendicular to the duct axis also shows the vortex flow, which was similarly observed in the previous case. The stream starts from the upper part of the throttle valve and passes down to the central area of the duct and flows into the lower part of the throttle valve. Then, it leaves the lower part of the throttle valve and flows into the upper part of the throttle valve, along the inner wall of the duct. As shown in Fig. 8(d), however, there is only one vortex flow compared with the three vortex flows in Fig. 6(d). This fact shows that, as the open angle of the throttle valve increases gradually, a single vortex line is formed along the duct. Fig. 9 shows the contours of the static pressure and the turbulence kinetic energy at an open angle of 30°. Compared

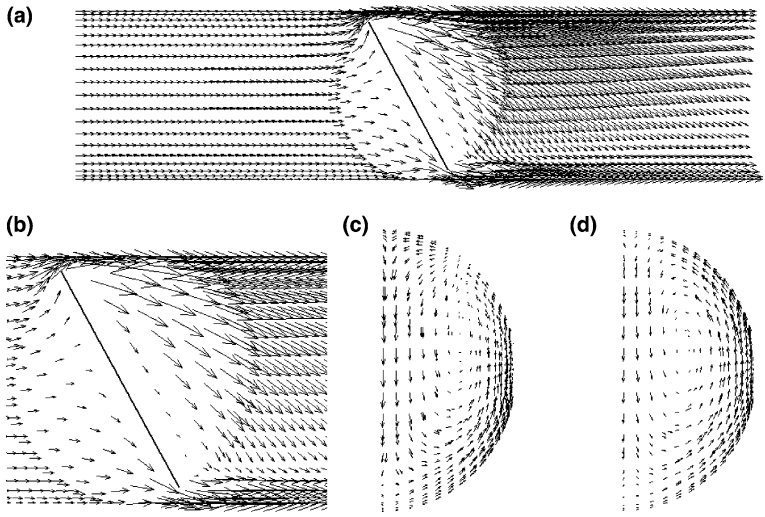

Fig. 8. Velocity distribution of airflow when the throttle valve is opened to 30° (maximum velocity = 142.5 m/s): (a) at the plane $y_2 = 0$, (b) zoomed plot, (c) at the plane $y_1 = 0.03$ m and (d) at the plane $y_1 = 0.06$ m.

with that of 20°, the pressure appears to increase gradually in the area downstream from the throttle valve. It can be found that the largest turbulent flow regions coincide with the zones where the two streams from both the upper and lower parts of the throttle mix and merge.

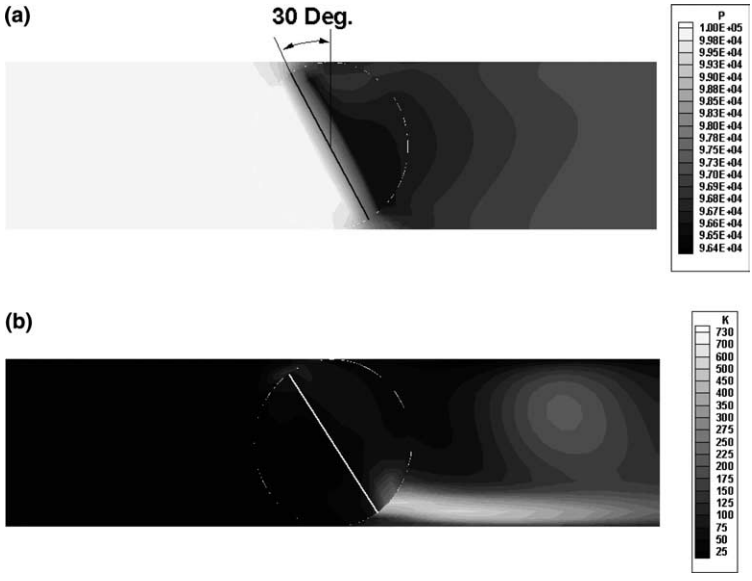

Fig. 9. Distributions of (a) pressure and (b) turbulence kinetic energy at the symmetric plane $y_2 = 0$ at the open angle of 30°.

Figs. 10(a) and (b) show the distribution of velocity vectors for the airflow at a longitudinal cross-section passing through the duct axis when the throttle is opened to 40°. The velocity distribution in this case is different from the previously seen cases in that the airflow around the throttle valve goes almost parallel to the wall of the throttle, causing the reverse flow from the lower part of the throttle to disappear. This flow pattern is due to the fact that, as the open area is increased, the airflow passes more smoothly through the gap between the throttle and the inner-surface of the conduit. Fig. 11 presents the contours of the static pressure and the turbulence kinetic energy at an open angle of 40°. The maximum of the turbulence kinetic energy is decreased to a value 30% lower than those of previous two cases.

Figs. 12(a) and (b) show the distribution of the velocity vectors for airflow at a longitudinal cross-section passing through the duct axis when the throttle is opened to 50°. The flow speed vector diagram shows that the velocities of airflows passing through the upper and lower parts of the throttle valve are suddenly decreased when compared with those of previous cases. Although the flow vector diagram of a cross-section perpendicular to the duct axis shows that the eddy resulting form the whirling airflow still exists, the magnitude of the vortex is also rapidly constricted. Fig. 13 presents the contours of the static pressure and the turbulence kinetic energy at the open angle of 50°. The pressure increases gradually as the fluid moves into the area downstream of the throttle valve. However, the magnitude of the turbulence kinetic energy decreases significantly compared with the previous three cases. This trend continues as the open angle is increased beyond 50°.

Through all of the flow patterns at each open angle, it can be found that the anti-symmetric vortex lines are formed in the downstream region after the airflow passes through the throttle valve. This generation of the anti-symmetric vortex lines is a

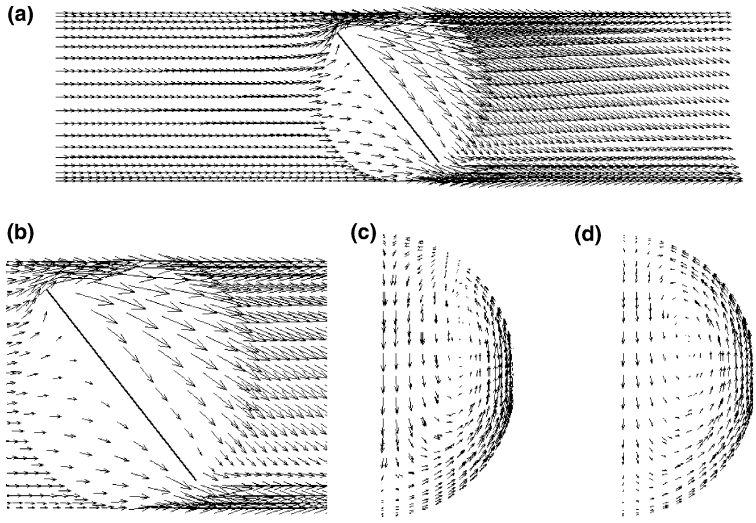

Fig. 10. Velocity distribution of airflow when the throttle valve is opened to 40 ° (maximum velocity = 112.9 m/s): (a) at the plane $y_2 = 0$, (b) zoomed plot, (c) at the plane $y_1 = 0.03$ m and (d) at the plane $y_1 = 0.06$ m.

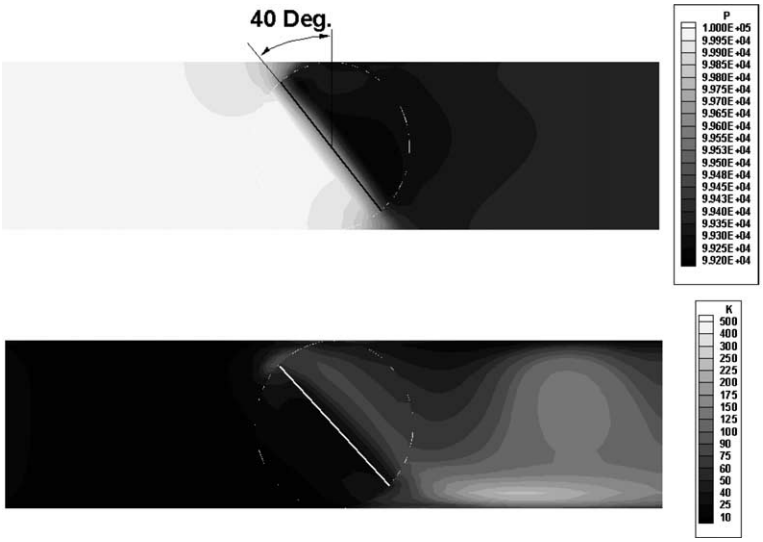

Fig. 11. Distributions of (a) pressure and (b) turbulence kinetic energy at the symmetric plane $y_2 = 0$ at the open angle of 40°.

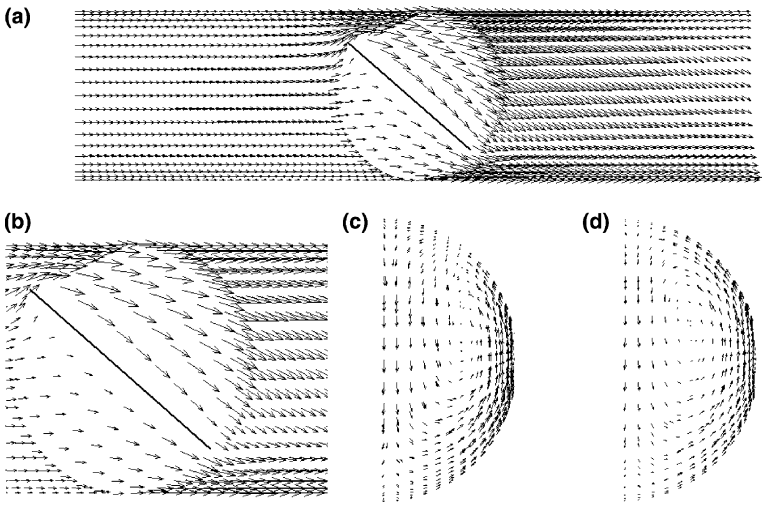

Fig. 12. Velocity distribution of airflow when the throttle valve is opened to 50° (maximum velocity = 68.97 m/s): (a) at the plane $y_2 = 0$, (b) zoomed plot, (c) at the plane $y_1 = 0.03$ m and (d) at the plane $y_1 = 0.06$ m.

large-scale motion that feeds the turbulence. This anti-symmetric vortex therefore can be referred to as the main mechanism for generating noise from the quick-opening throttle valve. A more detailed description is given in Section 4.

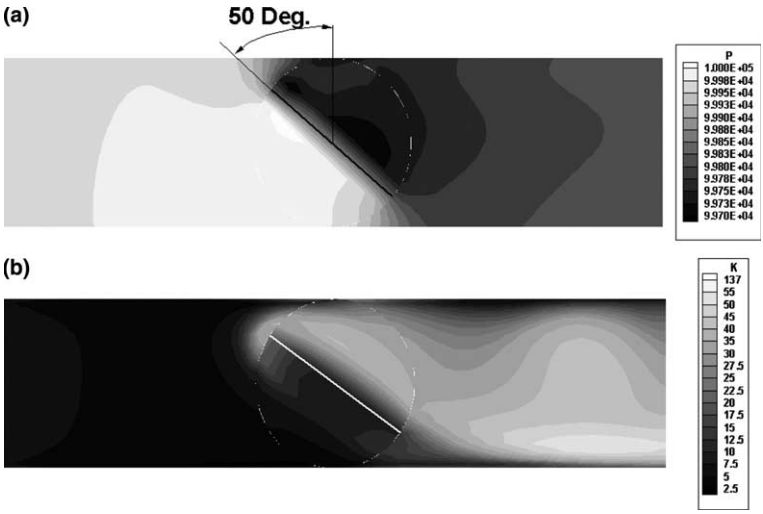

Fig. 13. Distributions of (a) pressure and (b) turbulence kinetic energy at the symmetric plane $y_2 = 0$ at the open angle of 50°.

3.2. Prediction of internal aerodynamic noise

In this section, the internal aerodynamic noise from the quick-opening throttle valve is predicted by combining the semi-analytic model and the previously calculated flow data. Table 1 shows the cut-on frequencies for each mode of the conduit containing a throttle valve. From this table, we can see that the components below 4150 Hz are cut-off and only (0, 1) mode, i.e., the plane wave is propagated. The time step in the previous flow simulation is 0.0002 s and therefore the Nyquist frequency is 2500 Hz. Thus, in the present noise prediction with previously calculated flow data, only the plane mode is valid. This means that the spatial derivatives of the y_1-direction in Eqs. (15) and (16) are only non-zero for (0, 1) mode. In other words, only the f_1 and T_{11} terms in Eqs. (15) and (16) make contribution to the acoustic pressure in the plane mode. It is evident that, as the time step in the flow simulation is lowered, the Nyquist frequency is increased more, and thus the effective range of frequency in predicted noise levels is also extended to higher frequencies. However, in the present calculation, unsteady numerical cost limits the allowable time resolution in flow simulation.

Prediction of intake noise from the quick-opening throttle valve is carried out by using Eqs. (7), (15) and (16). From a physical point of view, computation of Eqs. (7), (15) and (16) may be considered to be a filtering process, where dipole sources of unsteady pressure on the surface of the throttle valve and quadrupole sources of turbulent velocities in flow field are filtered with the Green function determined by the geometry of the duct through time and space integration. Fig. 14 shows the predicted flow quantities related to the dipole source of Eq. (15) at the open angle of 5°. Fig. 14(a) shows the pressure distribution on the surface of the throttle valve. Fig. 14(b)

Table 1
Inflection points of J_m: $J'_m(x_{mn}) = 0$ and cut-on frequency for each mode

m	n					f_{mn} (Hz)	cx_{mn}/r
	1	2	3	4	5		
0	0	3.83	7.02	10.17	13.32	f_{01}	0
1	1.84	5.33	8.54	11.71	14.86	f_{11}	4150
2	3.05	6.71	9.97	13.17	16.35	f_{21}	6880
3	4.20	8.02	11.35	14.59	17.79	f_{02}	8639
4	5.32	9.28	12.68	15.96	19.20	f_{31}	9474
5	6.41	10.52	13.99	17.31	20.58	f_{41}	12000

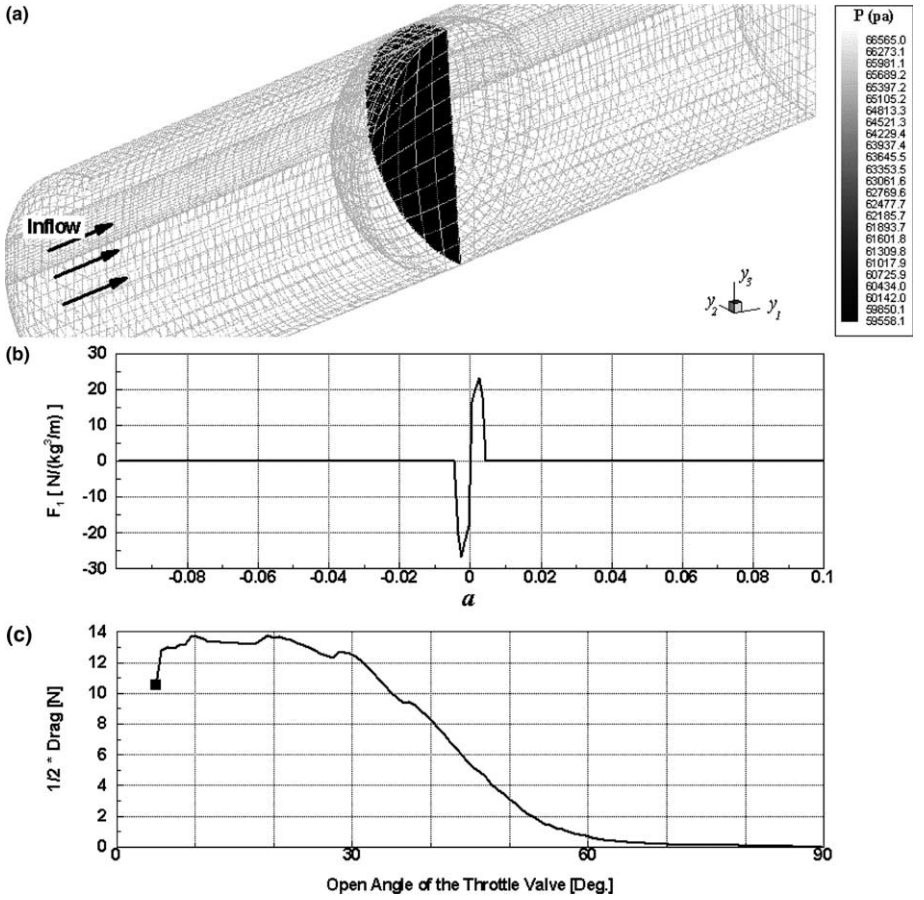

Fig. 14. The dipole sources of airflow when the throttle valve is opened to 5°: (a) pressure distribution on the surface of the throttle valve, (b) variation of $\mathbf{F}_1$ along the direction of flow stream and (c) the drag of the throttle valve.

shows the variations of $\mathbf{F}_1$ along the streamwise direction. The $\mathbf{F}_1$ term is defined as follows:

$$F_1(a = \mathrm{i}\Delta y_1) = \int_{a-0.5\Delta y_1}^{a+0.5\Delta y_1} \int_0^{2\pi} \int_0^{r_d} f_1(\mathbf{y}, \tau) r \,\mathrm{d}r \,\mathrm{d}\theta \,\mathrm{d}y_1, \tag{17}$$

where $\Delta y_1 = 0.001$ and $i = -100, -99, \ldots, -1, 0, 1, \ldots, 99, 100$. At this initial open angle, the distribution of $\mathbf{F}_1$ is found to be concentrated on the $y_1 = 0$ plane, which includes the rotation axis of the throttle vale, and perpendicular to the duct axis. The distribution of $\mathbf{F}_1$ in time and space is utilized for computing the dipole-originated and plane-mode acoustic signal using Eqs. (7) and (15). Fig. 14(c) shows the drag of the throttle valve. The line on this figure shows the complete variation of the drag during the full opening process, with the drag at this opening angle marked by the

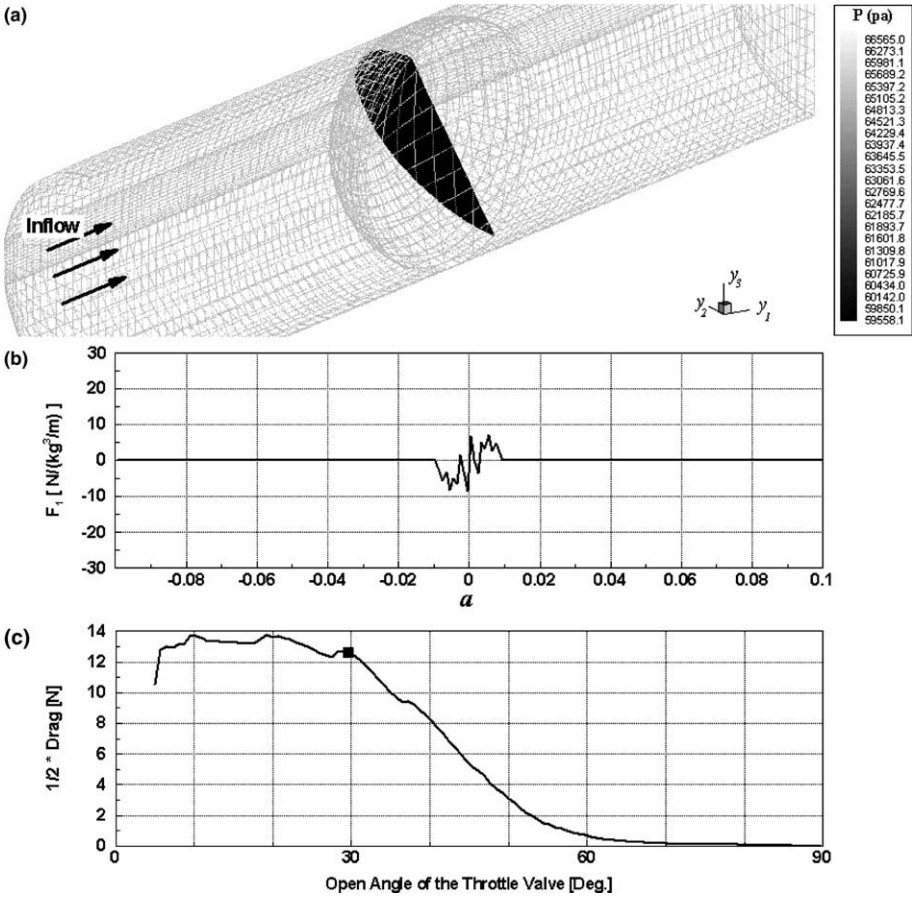

Fig. 15. The dipole sources of airflow when the throttle valve is opened to 30°: (a) pressure distribution on the surface of the throttle valve, (b) variation of $\mathbf{F}_1$ along the direction of flow stream and (c) the drag of the throttle valve.

filled rectangle. Fig. 15 shows the same types of plots when the throttle valve is opened to the 30°. The distribution of $\mathbf{F}_1$ is more elongated along the flow stream direction as the throttle valve is opened more. The drag of the throttle at the open angle of 30° is on the verge of declination after passing through the maximum region of the drag. Fig. 16 presents the same types of plots at the open angle of 50°. The distribution of $\mathbf{F}_1$ is more widely expanded than the previous cases. The drag of the throttle is also rapidly decreased.

Fig. 17 presents the predicted flow quantities related to the quadrupole source of Eq. (16) at the open angle of 5°. Fig. 17(a) shows the variation of turbulence kinetic energy over the entire computation domain. Fig. 17(b) shows the distribution of the integrated Lighthill stress tensor $\mathbf{T}_{11}$ along the streamwise direction. The terms $\mathbf{T}_{11}$ defined as follows:

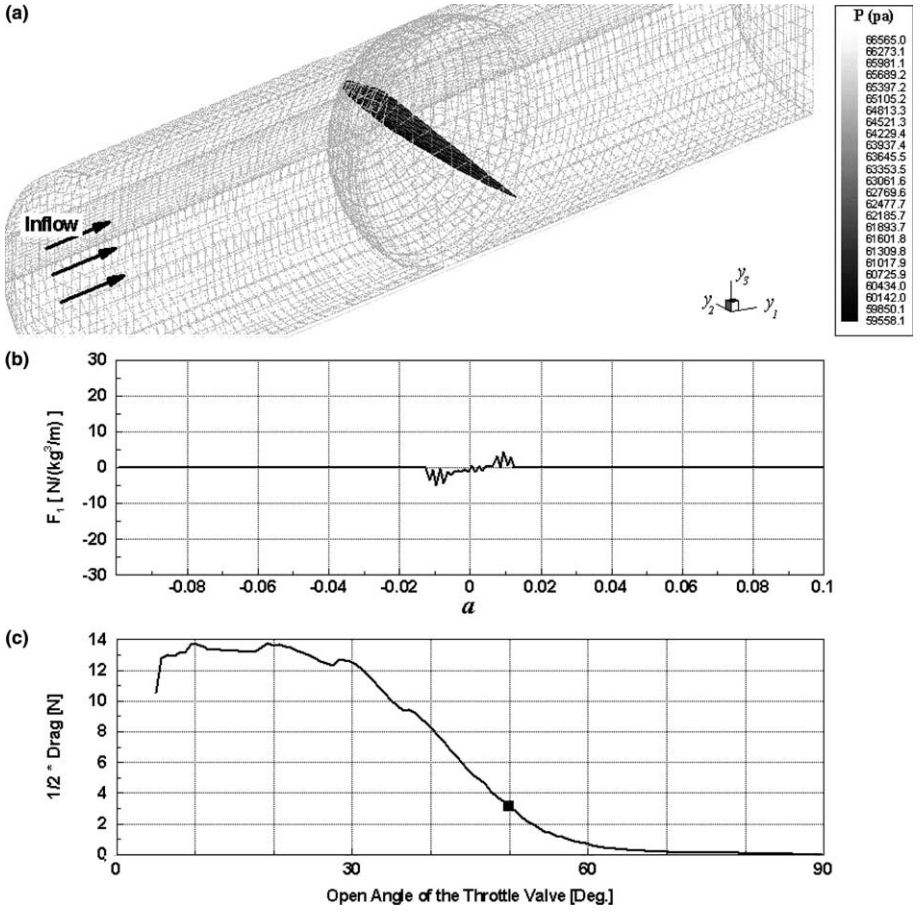

Fig. 16. The dipole sources of airflow when the throttle valve is opened to 50°: (a) pressure distribution on the surface of the throttle valve, (b) Variation of $\mathbf{F}_1$ along the direction of flow stream and (c) the drag of the throttle valve.

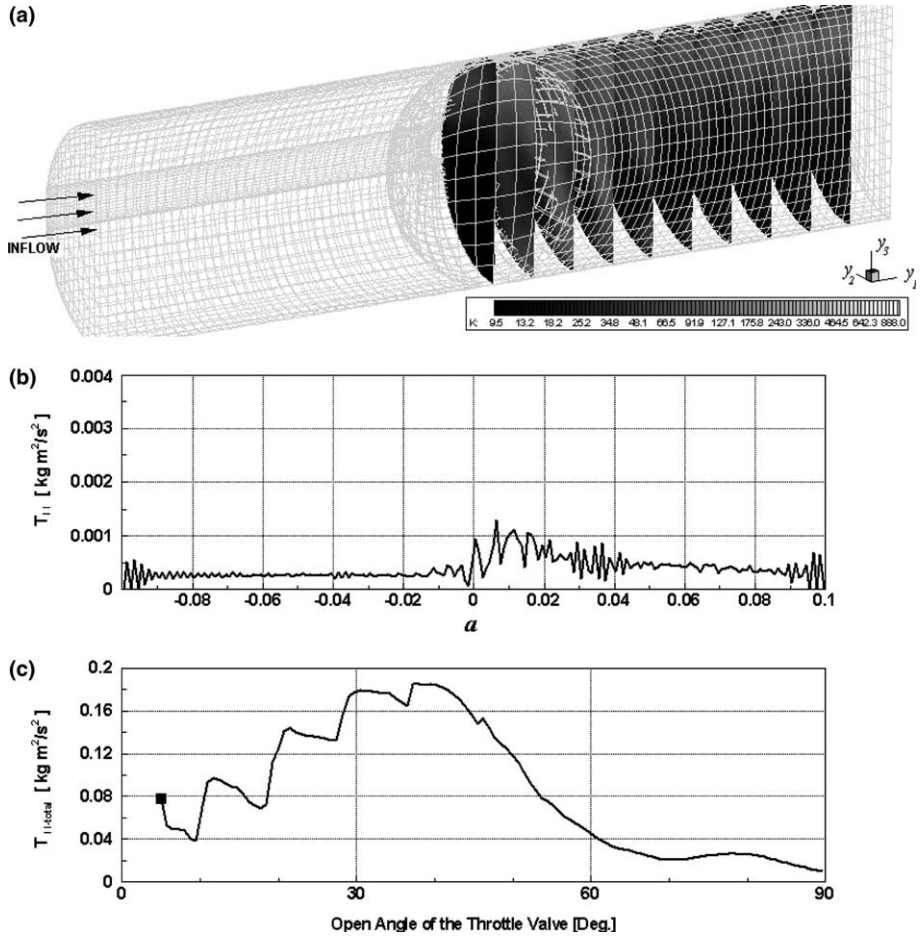

Fig. 17. The quadrupole sources of airflow when the throttle valve is opened to 5°: (a) the variation of turbulence kinetic energy over whole computation domain, (b) the distribution of $\mathbf{T}_{11}$ along the flow-stream direction, and (c) space-integrated values of T_{11} over whole computation domain.

$$\mathbf{T}_{11}(a = \mathrm{i}\Delta y_1) = \int_{a-0.5\Delta y_1}^{a+0.5\Delta y_1} \int_0^{2\pi} \int_0^{r_d} T_{11}(\mathbf{y}, \tau) r \, \mathrm{d}r \, \mathrm{d}\theta \, \mathrm{d}y_1, \tag{18}$$

where $\Delta y_1 = 0.001$, $i = -100, -99, \ldots, -1, 0, 1, \ldots, 99, 100$ and $T_{11} = \rho u_1 u_1$. Here, $\mathbf{T}_{11}$ is utilized to calculate the quadrupole-originated, plane-mode noise signal. At this initial stage, strong fluctuation of $\mathbf{T}_{11}$ is dominant behind the throttle valve. Fig. 17(c) shows the space-integrated values of T_{11} over the entire computation domain at the open angle of 5°. The line on this figure shows the complete variation of the space-integrated value of T_{11} during the entire opening process, with the value at this opening angle marked by the filled rectangle. Fig. 18 shows the same plot when the throttle valve is opened to the 30°. From this figure, it is found that most of the downstream region behind the throttle is filled with the strong turbulence having

high turbulent kinetic energy, and that $\mathbf{T}_{11}$ also has a very high value over the range from $y_1 = -0.01$ m to $y_1 = 0.05$ m. The total integrated value of T_{11} is also located at the maximum region throughout the whole variation of T_{11}. Fig. 19 shows the same plots when the throttle valve is opened to the 50°. At this stage, as the passage area between the throttle valve and the inner surface of the conduit is further increased, the air streams pass more smoothly through the gap, and consequently, the integrated value of T_{11} is sharply decreased. The integrated value of T_{11} at 60° is approximately one-fifth of the maximum value at approximately 38°. From Figs. 17–19, we can see that there are some fluctuations in the inlet and outlet regions due to the inflow and outflow boundary conditions. However, some test cases where the boundaries are more extended than the present case confirm that the contribution of these fluctuations to the total values can be neglected.

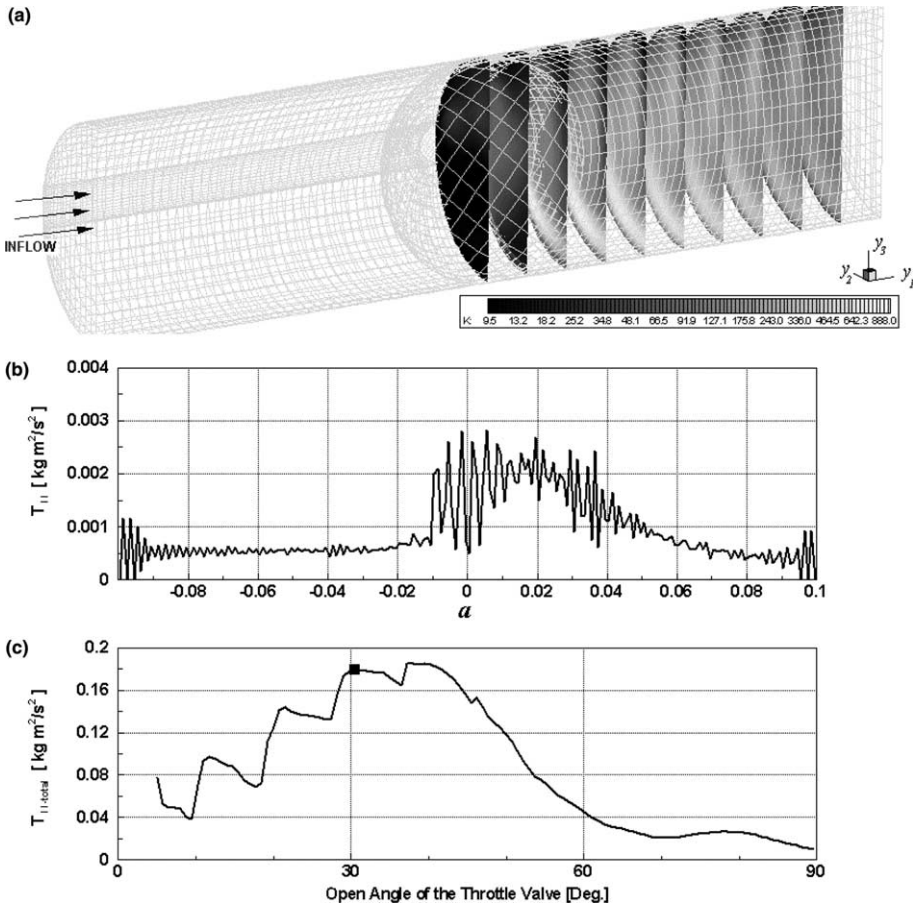

Fig. 18. The quadrupole sources of airflow when the throttle valve is opened to 30°: (a) the variation of turbulence kinetic energy over whole computation domain, (b) the distribution of $\mathbf{T}_{11}$ along the flow-stream direction, and (c) space-integrated values of T_{11} over whole computation domain.

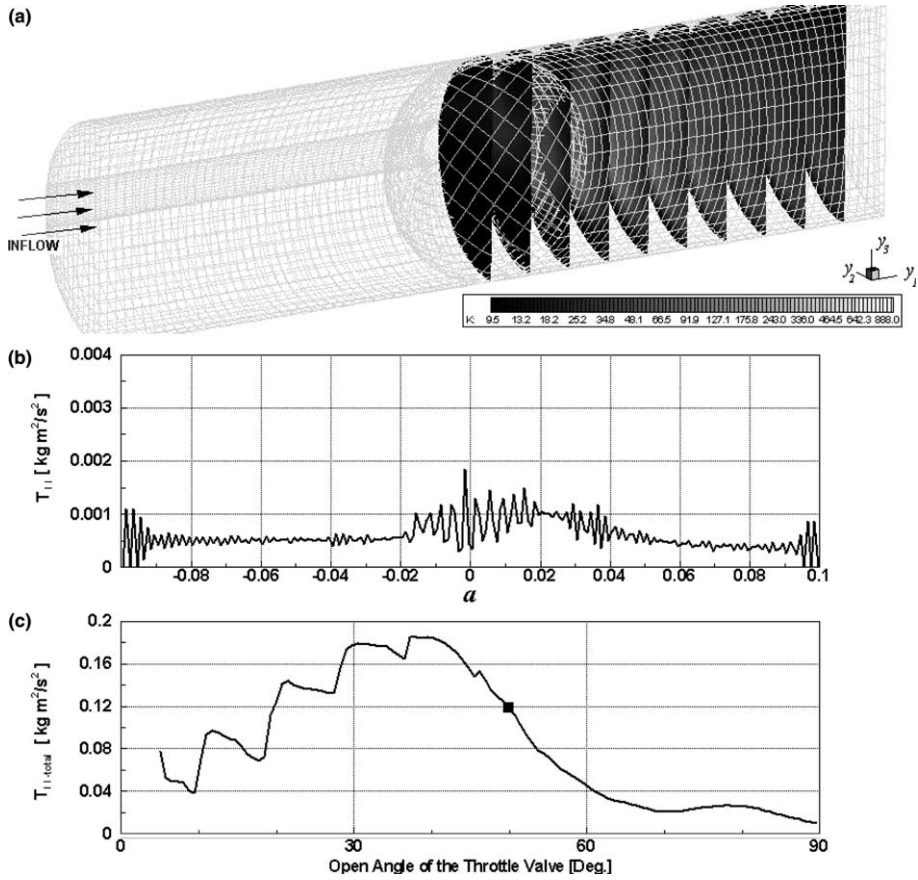

Fig. 19. The quadrupole sources of airflow when the throttle valve is opened to 50°: (a) the variation of turbulence kinetic energy over whole computation domain, (b) the distribution of $\mathbf{T}_1$ along the flow-stream direction and (c) space-integrated values of T_{11} over whole computation domain.

Frequency-domain acoustic pressure levels are predicted with Eqs. (7), (15) and (16) with the given source data in the space-time domain. Eq. (7) includes the infinite time-domain integration. However, because we are dealing with the transient problem the source event is assumed to take place within the time interval between 0 and 0.227 s. Therefore it seems to be reasonable that the source fluctuation is assumed to be zero outside this time interval. Fig. 20 shows a comparison of the predicted and measured noise level in the frequency band from 88 to 1760 Hz at the position of $x_1 = 190$ mm which is the measured point in the experiment. In this frequency range, plane mode is the only cut-on mode. This figure shows that the noise level from the dipole sources is larger than that from the quadrupole sources. From this fact, it can be deduced that the dipolar sound is dominant in the acoustic field from the quick-opening throttle valve. We also found that, although the discrepancy between the predicted results from dipole sources and the measured values is approximately 8

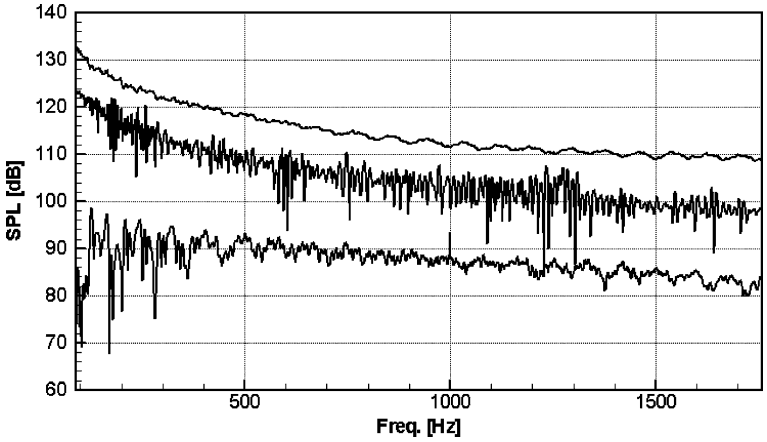

Fig. 20. Comparison of sound pressure levels at the position $y_1 = 0.190$ m: (upper) predicted results by using the dipole source, (middle) measured data, and (lower) predicted results by using the quadrupole source.

dB at each frequency, the decreasing trend of the predicted noise level according to the frequencies agrees well with that of the experimental results. For the complete frequency range, the predicted noise level was found to be greater than the measured, i.e., the simulation results normally overpredict. This is because the cross-sectional area of the pipe suddenly changes as the airstreams flow from the duct containing the throttle valve to the manifold where the measurement is taken. From a theoretical analysis [17], the relation between the strength, I, of the incident harmonic pressure wave and the strength, T, of the transmitted wave can be described as follows:

$$T = \frac{2A_1}{A_1 + A_2} I, \tag{19}$$

where A_1 and A_2 are the areas of incident duct and transmitted duct, respectively. In this case, A_1 is the area of the conduit containing the throttle valve, $\pi \times 0.024^2$ [m^2] and A_2 is that of the manifold, 0.0796×0.0735 [m^2]. Insertion of these areas into Eq. (19) leads to the transmission loss -6.5 dB. Fig. 21 shows the sound pressure levels of the original prediction, the corrected prediction by using the transmission loss, and the measured data on one-third octave band frequencies. The predicted noise level after the correction agrees reasonably well with the measured level.

4. Discussion

In this section, some issues on the relationship between the characteristics of generated noise as the result of estimation and the predicted flow characteristics during the quick-opening behavior are described. To compare the characteristics of transient flow around the throttle valve during the quick-opening behavior, with that

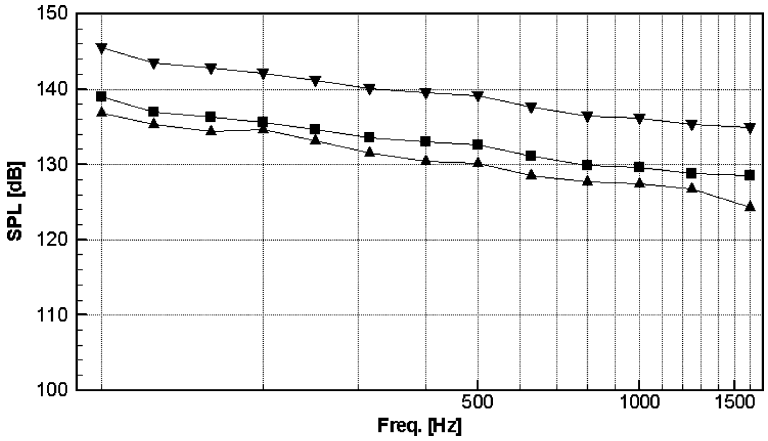

Fig. 21. Comparison of sound pressure levels at one-third octave band frequencies at the position $y_1 = 0.190$ m. (prediction result: ▼, corrected prediction result by using the transmission loss: ■ and measured data: ▲).

of steady flow around the throttle valve of which the open angle is kept constant at each angle, additional steady simulations were also carried out. It is noted that the steady simulations were performed with the outlet boundary condition of the static pressure corresponding to the measured value at each open angle shown in Fig. 4. Fig. 22 shows the comparisons of the distribution of turbulence kinetic energy in the symmetric plane ($y_2 = 0$), between the transient and steady simulations at each corresponding valve angle. In the results of steady simulations, the strong turbulence kinetic energy is observed to be located in the upper and lower regions just behind the gaps between the throttle and the inner wall of the duct, and their distributions are similar to that in turbulent jet flow that streams out from the constant gap. The turbulence structures predicted in the unsteady simulations are essentially different from that in the steady flow simulations. After the initial stage of the open angle 15°, the strong turbulence kinetic energy is mainly located in the lower parts of duct where the streams from both the upper and lower parts of the throttle mix and merge as explained in Section 2.1. This difference is due to the fact that the flow stream in the steady simulations, like jet-flows, just pass over the throttle valve the open angle of which is fixed while the flow stream in the unsteady simulation is affected by the relative motion of the throttle valve to the airflow, i.e., by the inertia force of the throttle valve at previous times. This inertia force leads to the different structures of the turbulence velocity field and inevitably has effects on the generated noise. The unsteady static pressure of the throttle valve in the unsteady simulation includes the information of the force exerted by the throttle on the fluid, due to the relative motion of the throttle valve as well as the flow passing over throttle valve in a quasi-stationary manner.

Fig. 23 shows the distributions of the $\mathbf{F}_1$ and $\mathbf{T}_{11}$ terms in the space-time dimensions. As explained in the previous section, it can be found in Fig. 23(a)

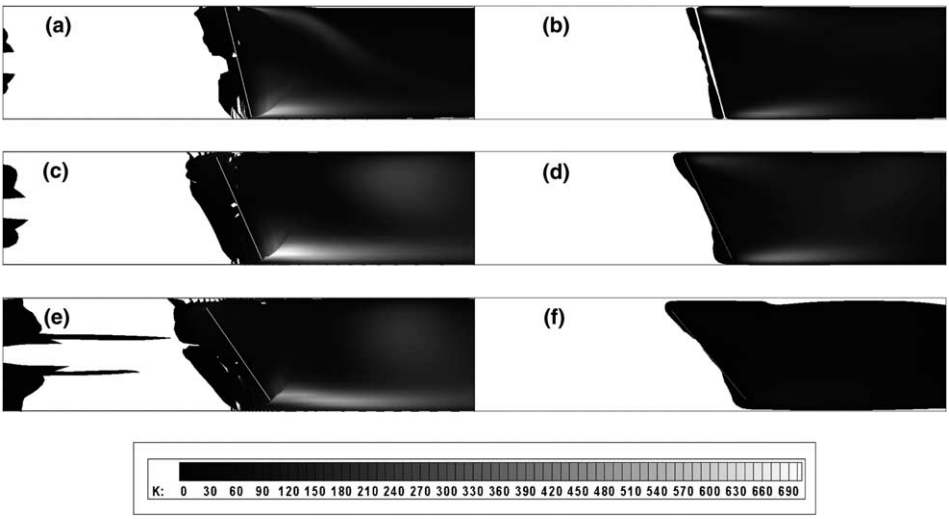

Fig. 22. Comparison of the distribution of the turbulence kinetic energy (k) in the symmetric plane ($y_2 = 0$) between the transient and steady simulations; (a) from the transient at 15° of the open angle, (b) from the steady at 15°, (c) from the transient at 25°, (d) from the steady at 25°, (e) from the transient at 35° and (f) from the steady at 35°.

that the distribution of $\mathbf{F}_1$ spreads out in the y_1-direction as the open angle of the throttle valve (or time) increases. The spreading shape in the time-space domain is determined by the opening angular speed of the throttle valve. If the angular speed is increased, it is evident that the spreading angle is also increased in the y_1-direction with the change of the fluctuating magnitude of $\mathbf{F}_1$. This distribution is directly input into Eqs. (15) and then (7), is then filtered with a Green function determined on the given frequency and mode, and finally contribute to the (0, 1) mode acoustic pressure in the frequency-domain. In this regard, it is evident that the angular speed affects the frequency characteristics and the magnitudes of the acoustic pressure through the variation of the spreading shape and magnitude of $\mathbf{F}_1$, respectively. Fig. 23(b) shows the distributions of the $\mathbf{T}_{11}$ terms in the space-time domain. Interestingly, the distribution of the quadrupole sources partially resembles that of the dipole sources. In this respect, the quadrupole sources seem to "remember" the opening action of the throttle valve. In fact, although the contribution of the quadrupole source to the acoustic field from the quick-opening throttle valve is negligible in comparison with that of the dipole source, this turbulent vorticity field indirectly contributes to the dipole sound through the energy transformation from the vortical to the acoustical by its scattering process on the solid wall. The dipole source distribution due to the unsteady loading of a body in a flow is simply a reaction to the force exerted by fluid on the body. In this respect, the dipole source can be considered as an essentially passive source. In order to provide a basic philosophy for the low-noise design, the detailed source

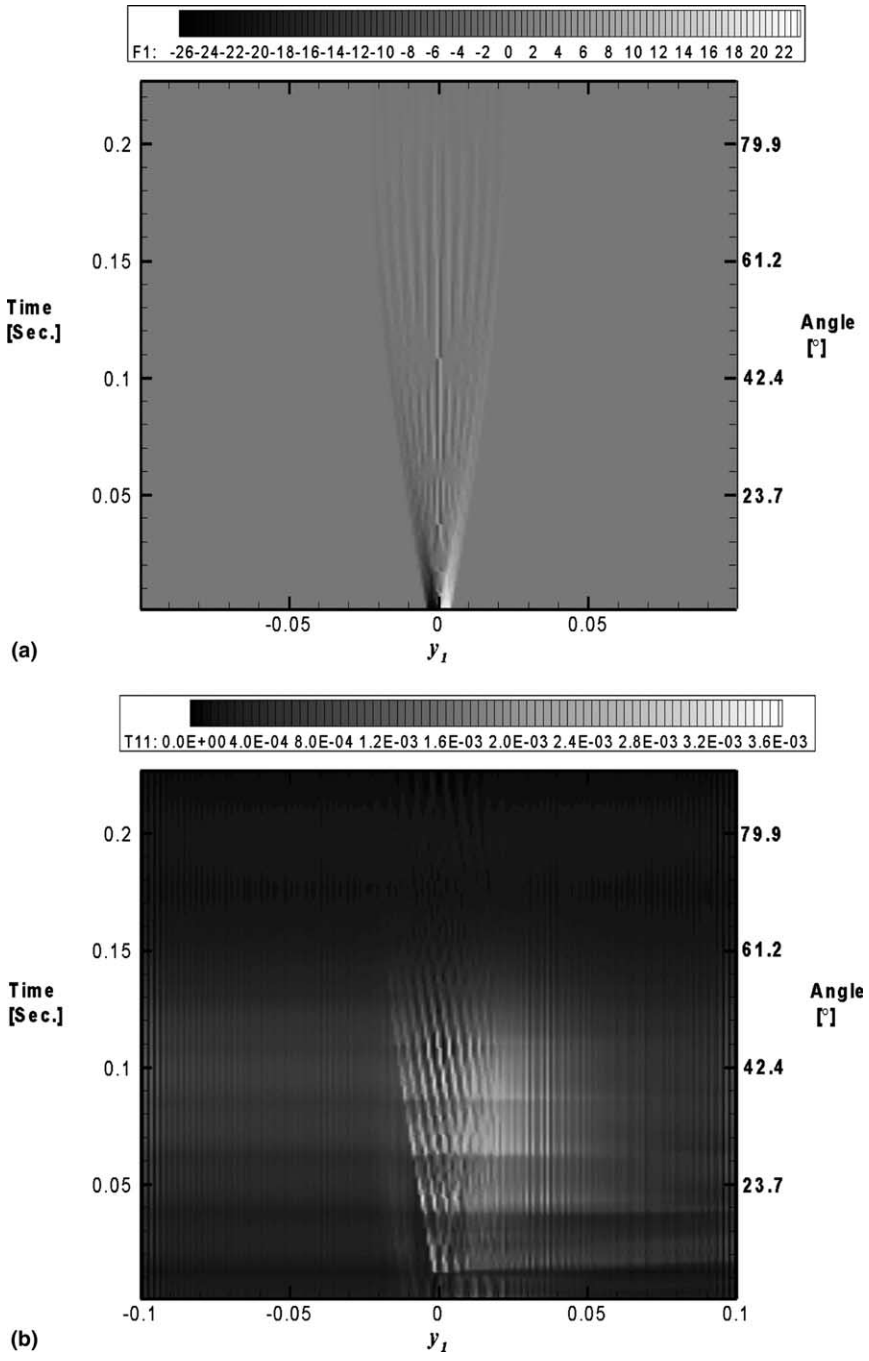

Fig. 23. Distributions of the modelled sources in the space and time domains: (a) the $\mathbf{F}_1$ term and (b) the $\mathbf{T}_{11}$ term.

mechanism must be identified. It can be seen from Fig. 23(b) that the strong quadrupole sources are distributed downstream of the throttle valve within approximately 20–50° angle-range. This prediction closely matches the measurement shown in Fig. 2 where the strong noise signal is generated when the throttle is opened within the 20–50° angle-range.

Fig. 24 presents the instantaneous spectra of the dipole noise computed with the Hanning window function with the width 0.013 s corresponding to 5° angle interval. From this figure, it can be found that the strong noise signal are produced between approximately 20° and 50° angle-range, which is also matching to those of the prediction of the quadrupole source distribution and of the measured noise signal. As given in the flow simulation results, it was found that anti-symmetric vortex lines were formed in the downstream direction after the airflow passes through the gap. This generation of the anti-symmetric vortex lines is a large-scale motion that feeds the turbulence. In addition to being the main quadrupole source in the Lighthill's stress tensor, turbulent vorticity also makes contributions to the dipolar sound by diffraction of the vorticity wave by the solid surface. Through the comparison of the instantaneous noise spectra and the time-space distribution of the quadrupole sources, we can infer that the main origin of aerodynamic noise generated from the quick-opening throttle valve could be attributed to anti-symmetric vortex lines.

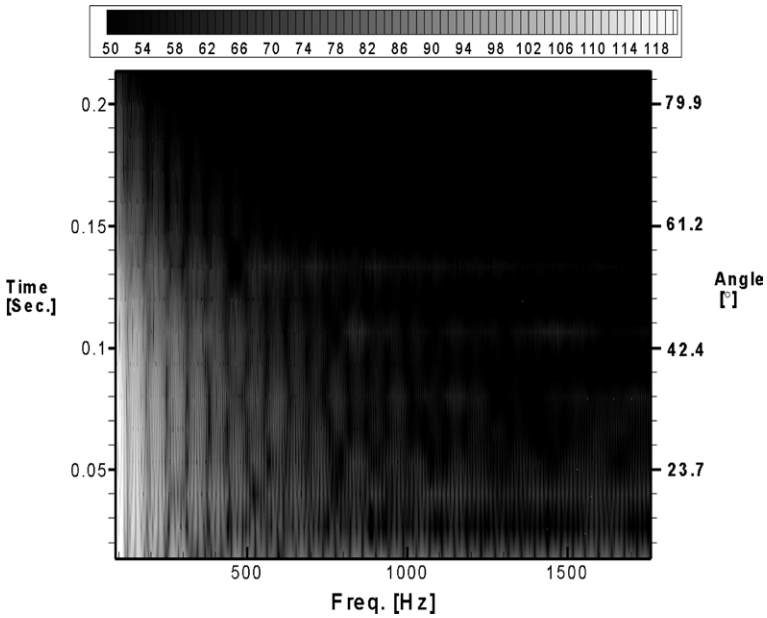

Fig. 24. The predicted instantaneous sound pressure level [dB] from the dipole sources.

5. Concluding remarks

The unsteady flow field from the quick-opening throttle valve was obtained by applying compressible CFD techniques, and its corresponding frequency-domain acoustic pressure was predicted by using the integral formula derived from the wave equation with the modelled source term by using the General Green Function. The predicted acoustic pressure levels show reasonable agreement with the measured data.

Through the comparison of the unsteady and steady flow simulations, it can be found that the turbulence structure in the steady flow simulation resembles that in general jet-flows while the turbulence structure in the unsteady simulation is mostly affected by the relative motion of the throttle to the airflow, i.e., by the inertia force of the throttle valve. Therefore, unsteady loading of the throttle valve in the unsteady simulation includes the information due to the relative motion of the throttle valve as well as due to the quasi-stationary flow passing through the throttle valve. This relative motion affects the distribution of unsteady loading in the space-time domain by the spreading shape and fluctuation magnitudes, which change the frequency characteristics and magnitude of the acoustic pressure.

The basic origin for generating the acoustic pressure from the quick-opening throttle valve can be attributed to the large coherent structure of the vortex lines formed in downstream, after the airflow passes over the throttle valve. Based on this finding, it can be inferred that low-noise design of the throttle-duct system can be made by using this concept to break this large-scale vortex structure.

Acknowledgements

This work was supported by the Post-doctoral Fellowship Program of Korea Science & Engineering Foundation (KOSEF) and by the Aerospace Technology Development Program of Ministry of Commerce, Industry and Energy. The authors acknowledge the contributions of J. Kim and K.T. Kang who were key contributors in the initial stages of this study.

Appendix A. General Green Function

The Fourier transform of G of Eq. (3) with respect to time, expressed as $g(\mathbf{x}, \mathbf{y}|\omega)$ satisfies the equation as follows:

$$\nabla^2 g - k^2 g = \delta(\mathbf{x} - \mathbf{y}) \tag{A.1}$$

and is related to G by the inverse transform,

$$G(x, t|y, \tau) = \frac{1}{2\pi} \int_{\infty}^{\infty} g(x, y|\omega) \exp\{-\mathrm{i}\omega(t - \tau)\} \, \mathrm{d}\omega. \tag{A.2}$$

The Green function is expressed as a sum of the normal modes of oscillation. First, consider the eigenfunction Ψ_{mn} satisfying the following 2D Helmholz equation and the boundary condition.

$$\left(\frac{\partial^2}{\partial y_2^2}+\frac{\partial^2}{\partial y_3^2}\right)\Psi_{mn}+\kappa_{mn}^2\Psi_{mn}=0 \quad \text{with} \quad \frac{\partial\Psi}{\partial n}=0 \quad \text{on the boundaries.} \tag{A.3}$$

The eigenfunction Ψ_{mn} satisfies the following orthonormal condition:

$$\int_A \Psi_{mn}^*\Psi_{m'n'}\,\mathrm{d}y_2\,\mathrm{d}y_3=\begin{cases}0 & \text{if } m\neq m' \text{ or } n\neq n'\\ \Gamma_{mn} & \text{if } m=m' \text{ and } n=n'\end{cases}, \tag{A.4}$$

where A is the cross-sectional area of a duct, the superscript asterisk denotes "complex conjugate", and $\Gamma_{mn}=\int_A|\Psi_{mn}|^2\,\mathrm{d}y_2\,\mathrm{d}y_3$.

Then, the solution of Eq. (A.1) can be assumed to be the sum of the product of the eigenfunction and the function of the y_1 as

$$g_\omega=\sum_{m,n=0}^{\infty} f_{mn}(y_1)\Psi_{mn}(y_2,y_3). \tag{A.5}$$

This form of solution automatically satisfies the wall boundary condition due to Eq. (A.3). Inserting (A.5) into (A.1) and using Eq. (A.2) leads to

$$\sum_{m,n=0}^{\infty}\left(\frac{\mathrm{d}^2}{\mathrm{d}y_1^2}+k_0^2-\kappa_{mn}^2\right)f_{mn}\Psi_{mn}=\delta(\mathbf{x}-\mathbf{y}). \tag{A.6}$$

Multiplying both sides of (A.6) by the conjugate of the eigenfunction, integrating the resultant equation on the area perpendicular to the duct axis, and using the relation of (A.4), the ordinary equation for f_{mn} can be obtained as follows:

$$\left(\frac{\mathrm{d}^2}{\mathrm{d}y_1^2}+k^2-\kappa_{mn}^2\right)f_{mn}=\frac{\Psi_{mn}^*(x_2,x_3)}{\Gamma_{mn}}\delta(\mathbf{x}-\mathbf{y}). \tag{A.7}$$

The solution of (A.7), approaching infinity, can be expressed as

$$f_{mn}=\frac{\mathrm{i}\Psi_{mn}^*(x_2,x_3)}{2k_{mn}\Gamma_{mn}}\exp\{\mathrm{i}k_{mn}|x_1-y_1|\}, \tag{A.8}$$

where

$$k_{mn}=\sqrt{k^2-\kappa_{mn}^2}. \tag{A.9}$$

By using Eq. (A.2), Green function in time-domain can be expressed as

$$\begin{aligned}G(\mathbf{x},t\mid\mathbf{y},\tau)&=\frac{\mathrm{i}}{4\pi}\sum_{m,n=0}^{\infty}\frac{\Psi_{m,n}(y_2,y_3)\Psi_{m,n}^*(x_2,x_3)}{\Gamma_{m,n}}\int_{-\infty}^{\infty}\frac{\exp\{\mathrm{i}k_{mn}\mid x_1-y_1\mid\}}{k_{m,n}}\\&\quad\times\exp\{-\mathrm{i}\omega(t-\tau)\}\,\mathrm{d}\omega.\end{aligned} \tag{A.10}$$

Appendix B. Coordinate transformation

Independent variables in Cartesian coordinates are expressed with those in cylindrical coordinates,

$$(y_1, y_2, y_3) = (y_1, r\cos\theta, r\sin\theta). \tag{B.1}$$

Then, first- and second-order spatial derivatives in Cartesian coordinate are transformed into those in cylindrical coordinates as follows:

$$\frac{\partial}{\partial y_2} = \frac{\partial r}{\partial y_2}\cdot\frac{\partial}{\partial r} + \frac{\partial\theta}{\partial y_2}\cdot\frac{\partial}{\partial\theta} = \cos\theta\cdot\frac{\partial}{\partial r} - \frac{\sin\theta}{r}\cdot\frac{\partial}{\partial\theta}, \tag{B.2}$$

$$\frac{\partial}{\partial y_3} = \frac{\partial r}{\partial y_3}\cdot\frac{\partial}{\partial r} + \frac{\partial\theta}{\partial y_3}\cdot\frac{\partial}{\partial\theta} = \sin\theta\cdot\frac{\partial}{\partial r} + \frac{\cos\theta}{r}\cdot\frac{\partial}{\partial\theta}, \tag{B.3}$$

$$\begin{aligned}\frac{\partial^2}{\partial y_2^2} &= \left(\cos\theta\cdot\frac{\partial}{\partial r} - \frac{\sin\theta}{r}\cdot\frac{\partial}{\partial\theta}\right)\left(\cos\theta\cdot\frac{\partial}{\partial r} - \frac{\sin\theta}{r}\cdot\frac{\partial}{\partial\theta}\right)\\ &= \cos\theta\frac{\partial}{\partial r}\left(\cos\theta\cdot\frac{\partial}{\partial r}\right) - \cos\theta\frac{\partial}{\partial r}\left(\frac{\sin\theta}{r}\cdot\frac{\partial}{\partial\theta}\right) - \frac{\sin\theta}{r}\cdot\frac{\partial}{\partial\theta}\left(\cos\theta\cdot\frac{\partial}{\partial r}\right)\\ &\quad + \frac{\sin\theta}{r}\cdot\frac{\partial}{\partial\theta}\left(\frac{\sin\theta}{r}\cdot\frac{\partial}{\partial\theta}\right)\\ &= \cos^2\theta\frac{\partial^2}{\partial r^2} + \frac{2\cos\theta\sin\theta}{r^2}\frac{\partial}{\partial\theta} - \frac{2\cos\theta\sin\theta}{r}\frac{\partial^2}{\partial r\partial\theta} + \frac{\sin^2\theta}{r^2}\frac{\partial}{\partial r} + \frac{\sin^2\theta}{r^2}\frac{\partial^2}{\partial\theta^2},\end{aligned} \tag{B.4}$$

$$\begin{aligned}\frac{\partial^2}{\partial y_3^2} &= \left(\sin\theta\cdot\frac{\partial}{\partial r} + \frac{\cos\theta}{r}\cdot\frac{\partial}{\partial\theta}\right)\left(\sin\theta\cdot\frac{\partial}{\partial r} + \frac{\cos\theta}{r}\cdot\frac{\partial}{\partial\theta}\right)\\ &= \sin\theta\cdot\frac{\partial}{\partial r}\left(\sin\theta\cdot\frac{\partial}{\partial r}\right) + \sin\theta\cdot\frac{\partial}{\partial r}\left(\frac{\cos\theta}{r}\cdot\frac{\partial}{\partial\theta}\right) + \frac{\cos\theta}{r}\cdot\frac{\partial}{\partial\theta}\left(\sin\theta\cdot\frac{\partial}{\partial r}\right)\\ &\quad + \frac{\cos\theta}{r}\cdot\frac{\partial}{\partial\theta}\left(\frac{\cos\theta}{r}\cdot\frac{\partial}{\partial\theta}\right)\\ &= \sin^2\theta\frac{\partial^2}{\partial r^2} - \frac{2\sin\theta\cos\theta}{r^2}\frac{\partial}{\partial\theta} + \frac{2\sin\theta\cos\theta}{r}\frac{\partial^2}{\partial r\partial\theta} + \frac{\cos^2\theta}{r}\frac{\partial}{\partial r} + \frac{\cos^2\theta}{r^2}\frac{\partial^2}{\partial\theta^2},\end{aligned} \tag{B.5}$$

$$\begin{aligned}\frac{\partial^2}{\partial y_2\partial y_3} &= \left(\cos\theta\cdot\frac{\partial}{\partial r} - \frac{\sin\theta}{r}\cdot\frac{\partial}{\partial\theta}\right)\left(\sin\theta\cdot\frac{\partial}{\partial r} + \frac{\cos\theta}{r}\cdot\frac{\partial}{\partial\theta}\right)\\ &= \cos\theta\frac{\partial}{\partial r}\left(\sin\theta\cdot\frac{\partial}{\partial r}\right) + \cos\theta\frac{\partial}{\partial r}\left(\frac{\cos\theta}{r}\cdot\frac{\partial}{\partial\theta}\right) - \frac{\sin\theta}{r}\cdot\frac{\partial}{\partial\theta}\left(\sin\theta\cdot\frac{\partial}{\partial r}\right)\\ &\quad - \frac{\sin\theta}{r}\cdot\frac{\partial}{\partial\theta}\left(\frac{\cos\theta}{r}\cdot\frac{\partial}{\partial\theta}\right)\\ &= \cos\theta\sin\theta\frac{\partial^2}{\partial r^2} - \frac{\cos^2\theta - \sin^2\theta}{r^2}\frac{\partial}{\partial\theta} + \frac{\cos^2\theta - \sin^2\theta}{r}\frac{\partial^2}{\partial r\partial\theta} -\\ &\quad - \frac{\sin\theta\cos\theta}{r}\frac{\partial}{\partial r}\frac{\sin\theta\cos\theta}{r^2}\frac{\partial^2}{\partial\theta^2}.\end{aligned} \tag{B.6}$$

By using the above equations, spatial derivatives in Eqs. (15) and (16) are transformed into those in cylindrical coordinate as follows:

$$\left[\frac{\partial}{\partial y_2}\right]\left(J_m(\kappa_{m,n}r)\mathrm{e}^{-\mathrm{i}(m\theta+k_n y_1-\omega\tau)}\right)=\left[\cos\theta\cdot\frac{\partial}{\partial r}-\frac{\sin\theta}{r}\cdot\frac{\partial}{\partial\theta}\right]\times\left(J_m(\kappa_{m,n}r)\mathrm{e}^{-\mathrm{i}(m\theta+k_{mn}y_1-\omega\tau)}\right), \tag{B.7}$$

$$\left[\frac{\partial}{\partial y_3}\right]\left(J_m(\kappa_{m,n}r)\mathrm{e}^{-\mathrm{i}(m\theta+k_{mn}y_1-\omega\tau)}\right)=\left[\sin\theta\cdot\frac{\partial}{\partial r}+\frac{\cos\theta}{r}\cdot\frac{\partial}{\partial\theta}\right]\times\left(J_m(\kappa_{m,n}r)\mathrm{e}^{-\mathrm{i}(m\theta+k_{mn}y_1-\omega\tau)}\right), \tag{B.8}$$

$$\left[\frac{\partial^2}{\partial y_2^2}\right]\left(J_m(\kappa_{m,n}r)\mathrm{e}^{-\mathrm{i}(m\theta+k_{mn}y_1-\omega\tau)}\right)=\left[\begin{array}{c}\cos^2\theta\frac{\partial^2}{\partial r^2}+\frac{2\cos\theta\sin\theta}{r^2}\frac{\partial}{\partial\theta}\\ -\frac{2\cos\theta\sin\theta}{r}\frac{\partial^2}{\partial r\partial\theta}\\ +\frac{\sin^2\theta}{r^2}\frac{\partial}{\partial r}+\frac{\sin^2\theta}{r^2}\frac{\partial^2}{\partial\theta^2}\end{array}\right]\times\left(J_m(\kappa_{m,n}r)\mathrm{e}^{-\mathrm{i}(m\theta+k_{mn}y_1-\omega\tau)}\right) \tag{B.9}$$

$$\left[\frac{\partial^2}{\partial y_3^2}\right]\left(J_m(\kappa_{mn}r)\mathrm{e}^{-\mathrm{i}(m\theta+k_{mn}y_1-\omega\tau)}\right)=\left[\begin{array}{c}\sin^2\theta\frac{\partial^2}{\partial r^2}-\frac{2\sin\theta\cos\theta}{r^2}\frac{\partial}{\partial\theta}\\ +\frac{2\sin\theta\cos\theta}{r}\frac{\partial^2}{\partial r\partial\theta}\\ +\frac{\cos^2\theta}{r}\frac{\partial}{\partial r}+\frac{\cos^2\theta}{r^2}\frac{\partial^2}{\partial\theta^2}\end{array}\right]\times\left(J_m(\kappa_{mn}r)\mathrm{e}^{-\mathrm{i}(m\theta+k_{mn}y_1-\omega\tau)}\right) \tag{B.10}$$

$$\left[\frac{\partial^2}{\partial y_2\partial y_3}\right]\left(J_m(\kappa_{mn}r)\mathrm{e}^{-\mathrm{i}(m\theta+k_{mn}y_1-\omega\tau)}\right)=\left[\begin{array}{c}\cos\theta\sin\theta\frac{\partial^2}{\partial r^2}-\frac{\cos^2\theta-\sin^2\theta}{r^2}\frac{\partial}{\partial\theta}\\ +\frac{\cos^2\theta-\sin^2\theta}{r}\frac{\partial^2}{\partial r\partial\theta}\\ -\frac{\sin\theta\cos\theta}{r}\frac{\partial}{\partial r}-\frac{\sin\theta\cos\theta}{r^2}\frac{\partial^2}{\partial\theta^2}\end{array}\right]\times\left(J_m(\kappa_{mn}r)\mathrm{e}^{-\mathrm{i}(m\theta+k_{mn}y_1-\omega\tau)}\right). \tag{B.11}$$

References

[1] Nakase Y, Kanehara K, Ohara K, Yamamoto K, Miyaji Y. Flow noise reduction upon quick opening the throttle. SAE 2001-01-1429.

[2] Doak PE. Excitation, transmission and radiation of sound from source distributions in hard-walled ducts of finite length (I): the effects of duct cross-section geometry and source distribution space-time. J Sound Vib 1973;31:1–72.

[3] Davies HG, Ffowcs Williams JE. Aerodynamic sound generation in a pipe. J Fluid Mech 1968;32:765–78.

[4] Gordon CG. Spoiler-generated flow noise (I): the experiment. J Acoust Soc Am 1968;43:1041–8.
[5] Gordon CG. Spoiler-generated flow noise (II): results. J Acoust Soc Am 1969;45:214–23.
[6] Nelson PA, Morfey CL. Aerodynamic sound production in low speed flow ducts. J Sound Vib 1981;79:263–89.
[7] Oldham DJ, Ukopoho AU. A pressure-based technique for predicting regenerated noise levels in ventilation systems. J Sound Vib 1990;140(2):259–72.
[8] Lewy S. Computation of broadband noise radiated by a ducted fan. Int J Acoust Vib 2002;7(3):141–53.
[9] Polacsek C, Desbois-Lavergne F. Fan interaction noise reduction using a wake generator: experiments and computational aeroacoustics. J Sound Vib 2003;265:725–43.
[10] Lighthill MJ. On sound generated aerodynamically – I. General theory. Proc Roy Soc Ser A 1952;211:564–87.
[11] Curle N. The influence of solid boundaries upon aerodynamic sound. Proc Roy Soc Ser A 1955;231:505–14.
[12] Cheong C., Kim S., Kim J., Lee S. Development of hybrid methods for the prediction of internal flow-induced noise and its application to throttle valve noise in an automotive engine. In: Proceedings of the 18th International Congress on Acoustics, Kyoto, Japan, 4–9 April 2004.
[13] Leonard BP. A stable and accurate convective modeling procedure based on quadratic upstream interpolation. Comp Meth Appl Mech Eng 1979;19:56–98.
[14] Richtmeyer RD, Morton KW. Difference methods for initial-value problems. 2nd ed.. New York: Wiley-Interscience; 1967.
[15] Issa RI. Solution of the implicitly discretised fluid flow equations by operator-splitting. J Comp Phys 1986;62:40–65.
[16] Demirdzic I, Peric M. Space conservation law in finite volume calculations of fluid flow. Int J Numer Meth Fluids 1988;8:1037–50.
[17] Dowling AP, Ffowcs-Williams JE. Sound and sources of sound. London, England: Ellis Horwood Limited; 1983.